# Six-Dimensional Beam-Envelope Equations: An Ultrafast Computational Approach for Interactive Modeling of Accelerator Structures

M.D. Kelisani,[1,2,*] S. Barzegar,[2] P. Craievich,[3] and S. Doebert[1]

[1] *BE-RF Department, European Organization for Nuclear Research (CERN), Geneva, CH-1211 Switzerland*
[2] *Institute for Research in Fundamental Sciences (IPM), P.O. Box 19395-5531, Tehran, Iran*
[3] *Paul Scherrer Institute (PSI), Villigen, CH-5232 Switzerland*

(Received 3 October 2022; revised 1 March 2023; accepted 3 April 2023; published 3 May 2023)

The design and implementation of accelerators capable of providing high-quality bunches require precise and efficient online modeling tools. Current comprehensive beam dynamics studies are prohibitively costly and challenging to use for interactive system design. A precise high-speed method for beam dynamics analysis in accelerator components is presented and compared to the results of the conventional particle-in-cell codes. Using powerful mathematical techniques, the suggested method evaluates the temporal evolution of a bunch shape in six-dimensional (6D) phase space along the accelerators. The moment equations that govern the evolution of the bunch envelope in 6D phase space are introduced. The three-dimensional space-charge, external, and emittance forces are calculated to be fully analytically insensitive to different beam envelopes. Substituting the obtained forces into the beam-envelope equations establishes a set of six modified equations describing the beam dynamics using simple algebraic expressions. The whole solution considers the energy spread inherent to an electron beam. The model accuracy is demonstrated by studying beam transport through various components of an accelerator. Applying this analytical approach not only forms a style of physical thinking by indicating the factors that affect the behavior of the charged particle bunches but also has an ultrafast computational speed that is at least 3 orders of magnitude faster than that of particle tracking codes for designing today's linear accelerators. Finally, the model's feasibility is benchmarked for successfully designing a photoinjector for the advanced proton driven plasma wakefield acceleration experiment.

DOI: 10.1103/PhysRevApplied.19.054011

## I. INTRODUCTION

Beam dynamics studies are a powerful and reliable source to design high-performance accelerators and have an essential influence on the achievement of high-quality beams [1,2]. Analyzing charged-particle-beam behavior along accelerator components allows for the generation of high-quality, high-current, and very short bunches [3–5]. Providing straightforward and elegant methods to investigate beam dynamics seems critical for the development of current electron sources and reveals the next generation of them [6,7].

A detailed description of all particle trajectories in six-dimensional (6D) phase space is one of the most practical methods for studying beam dynamics [8,9]. This is an approved model for the interpretation of charged-particle-beam behavior and is extensively used in particle-in-cell base (PIC) codes like PARMELA [10] and ASTRA [11]. To find the optimum operating point for an accelerator, a sweeping algorithm is introduced, which relies on running a PIC code in several rounds of trial and error. These methods involve solving thousands of coupled differential equations of motion simultaneously, which makes them too slow for designing an interdependent system. In addition, they might screen the physics behind [12] and suffer from statistical errors, e.g., emittance estimation. However, the most important key parameter for the description of a beam in an accelerator line is measuring the general parameters of the beam, such as divergence and beam size. Therefore, introducing models that consider the entire beam as one but not individual particles, is highly recommended to analyze the physics ruling the bunch evolution along the accelerator line. Such models provide fast-running computational tools for analyzing beam dynamics and, consequently, designing modern accelerators. An appropriate approach

*mdayyani@cern.ch; mohsen.dayyani.kelisani@cern.ch

to reach this goal is using conventional beam-envelope equations [13].

The beam-envelope equations calculate the shape of the entire bunch by taking into account space-charge forces, beam emittance, and external forces. Generally, solving these equations and finding an appropriate expression, in terms of the overall beam parameters, is impossible, except for some special conditions. For instance, when the transverse bunch size is ignorable against its length. The axial forces are negligible and the bunch evolution can be studied in two dimensions, thus only variations of beam rms radii are considered. In this model, the space-charge forces are calculated independent of the beam distribution and are expressed in terms of the average bunch current through Sacherer's theorem [14]. The effect of energy spread, even in the case of nonlinear motions, is included using a set of appropriate canonical transformations on the conventional Hamiltonian of the system [15]. However, apart from the two-dimensional (2D) nature of this model, the model cannot lead to appropriate expressions for describing the evolutions of the bunch emittance and energy spread due to its inherent complexity. While the bunch length is comparable to its radius, one can approximate the bunch by an ellipsoid filled with uniformly distributed charged particles, ignoring the energy-spread effect (uniform ellipsoidal bunch model) [16]. Although the model studies the evolution of a bunch in three dimensions, it fails to reflect the nonlinear effects of the space-charge forces (due to the presence of nonuniformity in the bunch distribution) and the external forces on the bunch motion [17,18]. For bunches with nonuniform distribution, different techniques are suggested to derive the envelope equation in two dimensions. One of these models solves the space-charge forces in terms of what is called the space-charge coefficients [19]. This 2D model is very practical for space-charge-dominated beams. However, it fails in the quantitative description of the emittance forces and, moreover, the beam's energy-spread effect is totally neglected. Another frequently used model for nonuniform distributions is assuming the beam as many uniform cylindrical slices of equal lengths and different radii [20,21]. Each slice would be affected by the local external fields and its own space-charge field, separately. Although this model allows for resolving the beam shape by an envelope equation, it still calculates the emittance variations of the beam by tracking individual particle trajectories. In addition, it is appropriate for 2D problems, when the bunch distribution in transverse and longitudinal directions is nearly uniform for each cylindrical slice. This approach is employed widely in the HOMDYN code [22,23]. Studying the consequences of three-dimensional (3D) effects, e.g., asymmetry in beam shape or fields, the beam's energy spread and emittance calculations are quite significant for stable beam propagation along an accelerator lattice. Particle-tracking codes perform three-dimensional simulations, but this is a time-devouring process and suffers from statistical errors. Generating high-quality beams requires a model that can interpret general beam behavior precisely in an accelerator line and is fast enough for online modeling with the intention of tuning accelerator components. Thus, the evaluation of a fast simplified model for solving envelope equations seems inventible.

Here, a simplified analytical model for beam dynamics studies in accelerator components is presented that is much faster than simulation-based procedures and has good consistency with the simulation outcomes. The 6D envelope equations are established in real space and momentum space for a practical beam. The envelope equations are modified in 6D phase space by deriving the external forces, space-charge forces, and thermal pressure forces, in terms of beam sizes and their divergences. The space-charge forces are calculated in terms of beam size and divergence for a correlated 6D Gaussian distribution. It is verified that a Gaussian distribution is capable of estimating very accurately the temporal evolution of practical beams, regardless of their real envelope shapes along the accelerator line. The space-charge forces are expressed regarding certain coefficients that are labeled as the space-charge coefficients, which can suppress the time-consuming process of averaging the space-charge fields over the distribution of the particles in each time step. The external forces on the beam are expressed as some simple algebraic expressions for the different basic components of linear accelerators. Finally, a set of six coupled differential equations can describe the whole general beam parameters in 6D phase space. Thus, it is a very fast-running computational tool rather than PIC codes that calculate thousands of differential equations every time step. In addition, these differential equations easily inform us about the determinative factors that participate in the beam behavior through accelerator lines. The model takes six essential features into account. (1) It shows the evolution of rms beam size and rms beam divergence in 6D phase space in both linear and nonlinear regimes. (2) Correlations between the momenta and coordinates of the particles in the bunch are considered. (3) It calculates the space-charge forces analytically in terms of rms beam size and rms divergence. (4) It includes the beam's energy spread to implement the real average behavior of the beam particles in all fields. (5) It explains the interactions of particles in the beam with each other and with the external components within the accelerator by some simple algebraic expressions. (6) It is able to calculate the thermal pressure force (emittance) analytically with high accuracy.

To verify the accuracy of our model, the results are compared with those obtained with PIC codes. It is shown that the suggested model shows a very accurate approximation, regardless of the practical beam-envelope shape in 6D phase space. The suggested model represents an analytical approach for emittance variations; thus, this

would be an efficient tool for the challenging problem of emittance compensation along the injectors [24,25]. Since this model is an ultrafast tool that supports full beam dynamics analysis, it is the preeminent alternative to time-consuming particle-tracking codes. The high computational speed is measured as at least 3 orders of magnitude faster on standard personal computers, which makes it a realistic approach for online modeling of accelerators that can predict the beam behavior for accurate design.

Section II introduces the envelope equations in 6D phase space. Section III explains how to calculate the space-charge forces. In Sec. IV, external forces for a variety of applied external fields on a beam by accelerator components are obtained. In the last section, the represented analytical model is applied to design an ultrashort-bunch, high-current, and low-emittance $S+X$-band photoinjector for the advanced wakefield experiment (AWAKE) [26] very successfully.

## II. 6D ENVELOPE EQUATIONS

General beam parameters like beam size and beam divergence allow one to address the beam dynamics in accelerator structures. Thus, the beam-envelope equation plays an essential role. The envelope equations are directly inferred from averaging over ray equations [27,28]. The so-called ray equations determine the trajectory of individual particles with respect to a reference particle, which has energy $\gamma_0$, normalized velocity $\beta_0$, and momentum $p_0 = \gamma_0\beta_0$. Utilizing Lorentz equations in the presence of space-charge ($s$ superscript) and external ($e$ superscript) electric fields, $\vec{E} = \vec{E}^s + \vec{E}^e$, and magnetic fields, $\vec{B} = \vec{B}^s + \vec{B}^e$ yields

$$\gamma' = \frac{\eta\vec{E}\cdot\vec{\beta}}{\beta_0}, \tag{1}$$

$$\Delta u'' + \frac{{\gamma'}_0}{{p_0}^3}\beta_u = -\frac{\eta(\vec{E}\cdot\vec{\beta})\beta_u}{\gamma{\beta_0}^2} - \frac{(1-\hat{u}\cdot\hat{z})\eta^2c^2(\overrightarrow{B^{\mathrm{SM}}}\cdot\hat{z})^2\Delta u}{4\gamma^2{\beta_0}^2} + \frac{\eta(\vec{E}+\vec{\beta}c\times\vec{B}-(1-\hat{u}\cdot\hat{z})\vec{\beta}c\times\overrightarrow{B^{\mathrm{SM}}})\cdot\hat{u}}{\gamma{\beta_0}^2}, \tag{2}$$

with $\beta_u = \beta_0(\hat{u}\cdot\hat{z} + \Delta u')$. $u$ stands for $x$,$y$,$z$ coordinates; $\eta = q/mc^2$ is the particle-charge-to-mass ratio; $\gamma$ and $\vec{\beta}$ are the energy and normalized velocity of the charged particle, respectively; and $\overrightarrow{B^{\mathrm{SM}}}$ shows the solenoidal magnetic field. Derivatives are with respect to $z_0$, which is the position of the reference particle.

Multiplying Eqs. (1) and (2) by $\Delta u$ and averaging over the particles gives the envelope equation for the beam shape:

$$\sigma_u'' + \frac{\gamma_0{\gamma'}_0}{{\gamma_0}^2{p_0}^2}\sigma_u' = F_u^e + F_u^s + F_u^\varepsilon, \tag{3}$$

where $\sigma_u = \sqrt{\langle\Delta u^2\rangle}$ is the rms beam size in the $u$ direction. The terms on the right-hand side of Eq. (3) show generalized forces ($F$ type), including external $F_u^e$, space-charge $F_u^s$, and emittance $F_u^\varepsilon$ forces, that evolve the beam size in the $u$ direction, where

$$F_u^e = -\frac{\eta}{{\beta_0}^2\sigma_u}\left\langle\frac{(\overrightarrow{E^e}\cdot\vec{\beta})\beta_u\Delta u}{\gamma}\right\rangle - \frac{\eta^2c^2(1-\hat{u}\cdot\hat{z})}{4{\beta_0}^2\sigma_u}\left\langle\frac{(\overrightarrow{B^{\mathrm{SM}}}\cdot\hat{z})^2\Delta u^2}{\gamma^2}\right\rangle + \frac{\eta}{{\beta_0}^2\sigma_u}\left\langle\frac{(\overrightarrow{E^e}+\vec{\beta}c\times\overrightarrow{B^e}-(1-\hat{u}\cdot\hat{z})\vec{\beta}c\times\overrightarrow{B^{\mathrm{SM}}})\cdot\Delta u\hat{u}}{\gamma}\right\rangle, \tag{4}$$

$$F_u^s = -\frac{\eta}{{\beta_0}^2\sigma_u}\left\langle\frac{(\overrightarrow{E^s}\cdot\vec{\beta})\beta_u\Delta u}{\gamma}\right\rangle + \frac{\eta}{{\beta_0}^2\sigma_u}\left\langle\frac{(\overrightarrow{E^s}+\vec{\beta}c\times\overrightarrow{B^s})\Delta u\hat{u}}{\gamma}\right\rangle, \tag{5}$$

$$F_u^\varepsilon = \frac{{\Lambda_u}^2 - {\sigma_u'}^2}{\sigma_u}. \tag{6}$$

The resulting envelope equation describes the evolution of the rms size, $\vec{\sigma}$ ($\vec{\sigma} = \sigma_x\hat{x} + \sigma_y\hat{y} + \sigma_z\hat{z}$), of a beam under the influence of all involved generalized forces of the $F$ type ($\vec{F} = \overrightarrow{F^e} + \overrightarrow{F^s} + \overrightarrow{F^\varepsilon}$). The parameter $\Lambda_u = \sqrt{\langle\Delta u'^2\rangle}$ indicates the rms beam divergence in the $u$ direction.

From Eq. (3), two regimes of beam propagation can be identified: emittance dominated and space-charge dominated. A measure of the relative importance of space-charge effects versus emittance effects can be given by defining a new parameter: $\chi_u = F_u^s/F_u^\varepsilon$. If $\chi_u > 1$ ($\chi_u < 1$), the beam shows more space-charge effects (emittance dominated). For $\chi_u \gg 1$, the beam is space-charge dominated and the emittance effects can be neglected, while, for $\chi_u \ll 1$, the opposite is true.

On the other hand, it is possible to derive an equation for the evolution of the beam rms divergence in momentum space similar to the envelop equation for beam shape [Eq. (3)]. To achieve that goal, taking the derivative of $\langle \Delta u'^2 \rangle$ with respect to $z_0$ and substituting $\Delta u''$ from Eq. (2) gives

$$\frac{d\Lambda_u}{dz_0} + \frac{\gamma_0 \gamma'_0}{\gamma_0^2 p_0^2}\Lambda_u = G_u^e + G_u^s, \tag{7}$$

where $G_u^e$ and $G_u^s$ are the generalized forces that affect the beam rms divergence in the $u$ direction and are defined as

$$G_u^e = -\frac{\eta}{{\beta_0}^2 \Lambda_u}\left\langle \frac{(\vec{E^e}\cdot\vec{\beta})\beta_u \Delta u'}{\gamma}\right\rangle - \frac{\eta^2 c^2 (1-\hat{u}\cdot\hat{z})}{4{\beta_0}^2\Lambda_u}\left\langle \frac{(\overrightarrow{B^{\mathrm{SM}}}\cdot\hat{z})^2 \Delta u \Delta u'}{\gamma^2}\right\rangle + \frac{\eta}{{\beta_0}^2\Lambda_u}\left\langle \frac{(\vec{E^e} + \vec{\beta}c\times\vec{B^e} - (1-\hat{u}\cdot\hat{z})\vec{\beta}c\times\overrightarrow{B^{\mathrm{SM}}})\Delta u'\hat{u}}{\gamma}\right\rangle, \tag{8}$$

$$G_u^s = -\frac{\eta}{{\beta_0}^2\Lambda_u}\left\langle \frac{(\vec{E^s}\cdot\vec{\beta})\beta_u\Delta u'}{\gamma}\right\rangle + \frac{\eta}{{\beta_0}^2\Lambda_u}\left\langle \frac{(\vec{E^s} + \vec{\beta}c\times\vec{B^s})\Delta u'\hat{u}}{\gamma}\right\rangle. \tag{9}$$

Similar to Eqs. (3) and (7), this provides an envelope equation for the evolution of beam divergence, $\vec{\Lambda}$ ($\vec{\Lambda} = \Lambda_x\hat{x} + \Lambda_y\hat{y} + \Lambda_z\hat{z}$), under the influence of all involved generalized forces of the $G$ type ($\vec{G} = \vec{G^e} + \vec{G^s}$).

Equations (3) and (7) provide a complete set of differential equations for the calculation of the beam envelopes in the 6D phase space. However, the equations, except in some very special cases, cannot be solved fully analytically. In principle, the beam-envelope equations can be solved analytically if the averaged terms in Eqs. (4)–(6), (8), and (9) can be expressed in terms of the beam sizes, $\sigma_u$; divergences, $\Lambda_u$; and values of the electromagnetic fields at the location of the reference particle. Moreover, according to the conventional definition of beam emittance in the $u$ direction,

$$\varepsilon_u = \sqrt{\langle \Delta u^2\rangle\langle \Delta u'^2\rangle - \langle \Delta u \Delta u'^2\rangle} = \sigma_u\sqrt{{\Lambda_u}^2 - {\sigma_u}'^2}, \tag{10}$$

knowing the beam rms size and the beam rms divergence along the accelerator line leads to finding an expression for the emittance evolution of a beam without having knowledge of its individual particle trajectories. The beam rms size and rms divergence following from Eqs. (3) and (7) can be expressed as a function of $z_0$; thus, it is possible to calculate the emittance of the bunch along the beam orbit (note that $\varepsilon_{nu} \cong p_0\varepsilon_u$ indicates the normalized value of emittance).

To describe the properties of an electron beam in accelerator components considering the beam's energy spread is determinative. The effect of energy spread in this model is taken as a perturbation. We expand the terms $1/\gamma$, $1/\gamma^2$, $\beta_z/\gamma$, ${\beta_z}^2/\gamma$, and $1-{\beta_z}^2/\gamma$, in Eqs. (3)–(9) to the third order of perturbation. Using $\beta_u = \beta_0(\hat{u}\,\hat{z} + \Delta u')$, these terms can be expressed in terms of $\Delta x'$, $\Delta y'$, and $\Delta z'$, e.g.,

$$\frac{1}{\gamma} \cong \frac{1}{\gamma_0}\left\{1 - {p_0}^2\Delta z' - \frac{{p_0}^2{\gamma_0}^2}{2}\Delta z'^2 - \frac{{p_0}^4{\gamma_0}^2}{2}\Delta z'^3 - \frac{{p_0}^2}{2}(1+{p_0}^2\Delta z')(\Delta x'^2 + \Delta y'^2)\right\}. \tag{11}$$

Consequently, the required average values can be calculated perturbatively for any defined distribution of the particles.

Generally, we predict that the evolution of the average bunch parameters (e.g., bunch dimensions in 6D phase space) is independent of the detail of the bunch structure, at least to a good approximation. Thus, the general bunch parameters can be written as a function of the other ones, for instance, $\sigma_x = \sigma_x(\sigma_x, \sigma_y, \sigma_z, \Lambda_x, \Lambda_y, \Lambda_z)$. The idea is analogous to the hydrodynamic, where the general parameters of an ideal gas (like its pressure, $P$) are independent of the details of its structure and can be expressed in terms of the other parameters (like $P = NKT/V$). In the next sections, the validity of this practical approximation is

benchmarked and discussed by considering some practical examples.

## III. SPACE-CHARGE FORCES

To find an analytical solution for 6D envelope equations, it is necessary to establish the space-charge forces in terms of beam size, $\vec{\sigma}$, and divergence, $\vec{\Lambda}$. To reach this goal, we consider a correlated 6D Gaussian distribution. As proved in the following, a Gaussian distribution is capable of estimating very accurately the temporal evolution of practical beams, regardless of their real envelope shapes along the accelerator line.

The space-charge electromagnetic fields associated with a Gaussian distribution like $\rho_b = q_b\left(e^{-\left(\Delta x/\sqrt{2}\sigma_x\right)^2}/\sqrt{2\pi}\sigma_x\right)\left(e^{-\left(\Delta y/\sqrt{2}\sigma_y\right)^2}/\sqrt{2\pi}\sigma_y\right)\left(e^{-\left(\Delta z/\sqrt{2}\sigma_z\right)^2}/\sqrt{2\pi}\sigma_z\right)$ ($q_b$ is the total charge of the bunch) are

$$\overrightarrow{E^s} = \frac{q_b\gamma_0}{(2\pi)^{3/2}\epsilon_0}\times\int_0^{+\infty}\frac{e^{-(\Delta x^2/(2(2s+{\sigma_x}^2)))}e^{-(\Delta y^2/(2(2s+{\sigma_y}^2)))}e^{-({\gamma_0}^2\Delta z^2/(2(2s+{\gamma_0}^2{\sigma_z}^2)))}}{\sqrt{(2s+{\sigma_x}^2)(2s+{\sigma_y}^2)(2s+{\gamma_0}^2{\sigma_z}^2)}}$$
$$\times\left[\frac{\Delta x\hat{x}}{(2s+{\sigma_x}^2)}+\frac{\Delta y\hat{y}}{(2s+{\sigma_y}^2)}+\frac{\Delta z\hat{z}}{(2s+{\gamma_0}^2{\sigma_z}^2)}\right]ds, \tag{12}$$

$$\overrightarrow{B^s} = \frac{\beta_0}{c}\hat{z}\times\overrightarrow{E^s}, \tag{13}$$

where the completeness property of the eigenfunctions $e^{i\vec{k}\cdot\vec{r}}/2\pi^{3/2}$, i.e., $1/((x-x')^2+(y-y')^2+(z-z')^2)^{1/2} = 1/2\pi^2\int(e^{i\vec{k}\cdot(\vec{r}-\vec{r}')}/k^2)d^3k$, is used [29]. Then by substituting the space-charge fields into Eqs. (5) and (9) and averaging over the correlated 6D Gaussian distribution ($\mathcal{F} = \mathcal{F}_x\mathcal{F}_y\mathcal{F}_z$),

$$\mathcal{F}_u = \frac{p_0}{2\varepsilon_u}e^{-\left[\left(\left(p_0\Lambda_u/\sqrt{2}\varepsilon_u\right)\Delta u\right)^2-2(p_0{}^2\sigma_u\sigma_u'/2{\varepsilon_u}^2)\Delta u\Delta u'+\left(\left(p_0\Lambda_u/\sqrt{2}\varepsilon_u\right)\Delta u'\right)^2\right]}, \tag{14}$$

the space-charge force components up to the third order of perturbation can be written as

$$F_x^s \cong +\frac{f_b}{{\beta_0}^2{\gamma_0}^3}\times\frac{\alpha_x}{\sigma_x\sigma_z}-\frac{f_b}{\gamma_0}\left\{\frac{({\Lambda_x}^2+2{\sigma_x'}^2)\alpha_x-{\sigma_x'}^2\alpha_{xx}}{2\sigma_x\sigma_z}+\frac{8{\Lambda_y}^2\alpha_x-{\sigma_y'}^2\alpha_{xy}}{16\sigma_x\sigma_z}+\frac{(1-{p_0}^2)(2{\Lambda_z}^2\alpha_x-{\sigma'}^2{}_z\alpha_{xz})}{4\sigma_x\sigma_z}\right\}$$
$$-\frac{f_b}{\gamma_0}\left\{\frac{({\Lambda_x}^2+2{\sigma_x'}^2)\alpha_x-{\sigma_x'}^2\alpha_{xx}}{\sigma_x\sigma_z}+\frac{\sigma_x'\sigma_y'(8\alpha_y-\alpha_{xy})}{8\sigma_z\sigma_y}+\frac{(1-{p_0}^2)\sigma_x'\sigma_z'(2{\gamma_0}^2{\sigma_z}^2\alpha_z-\sigma_x\sigma_y\alpha_{xz})}{2\sigma_x\sigma_y{\gamma_0}^2{\sigma_z}^2}\right\}, \tag{15}$$

$$F_y^s \cong +\frac{f_b}{{\beta_0}^2{\gamma_0}^3}\times\frac{\alpha_y}{\sigma_y\sigma_z}-\frac{f_b}{\gamma_0}\left\{\frac{({\Lambda_y}^2+2{\sigma_y'}^2)\alpha_y-{\sigma_y'}^2\alpha_{yy}}{2\sigma_y\sigma_z}+\frac{8{\Lambda_x}^2\alpha_y-{\sigma_x'}^2\alpha_{xy}}{16\sigma_y\sigma_z}+\frac{(1-{p_0}^2)(2{\Lambda_z}^2\alpha_y-{\sigma_z'}^2\alpha_{yz})}{4\sigma_y\sigma_z}\right\}$$
$$-\frac{f_b}{\gamma_0}\left\{\frac{({\Lambda_y}^2+2{\sigma_y'}^2)\alpha_y-{\sigma_y'}^2\alpha_{yy}}{\sigma_y\sigma_z}+\frac{\sigma_y'\sigma_x'(8\alpha_x-\alpha_{xy})}{8\sigma_z\sigma_x}+\frac{(1-{p_0}^2)\sigma_y'\sigma_z'(2{\gamma_0}^2{\sigma_z}^2\alpha_z-\sigma_x\sigma_y\alpha_{yz})}{2\sigma_y\sigma_x{\gamma_0}^2{\sigma_z}^2}\right\}, \tag{16}$$

$$F_z^s \cong +\frac{f_b}{{\beta_0}^2{\gamma_0}^3}\times\frac{\alpha_z}{\sigma_x\sigma_y}-\frac{f_b}{\gamma_0}\left\{\frac{3(1-{p_0}^2)(2({\Lambda_z}^2+2{\sigma'}^2{}_z)\alpha_z-{\sigma'}^2{}_z\alpha_{zz})}{4\sigma_x\sigma_y}+\frac{2{\gamma_0}^2{\sigma_z}^2{\Lambda_x}^2\alpha_z-{\sigma_x'}^2\sigma_x\sigma_y\alpha_{xz}}{4\sigma_x\sigma_y{\gamma_0}^2{\sigma_z}^2}\right.$$
$$\left.+\frac{2{\gamma_0}^2{\sigma_z}^2{\Lambda_y}^2\alpha_z-{\sigma_y'}^2\sigma_x\sigma_y\alpha_{yz}}{4\sigma_x\sigma_y{\gamma_0}^2{\sigma_z}^2}\right\}-\frac{f_b}{\gamma_0}\left\{\frac{\sigma_x'\sigma_z'(2\alpha_x-\alpha_{xz})}{2\sigma_x\sigma_z}+\frac{\sigma_y'\sigma_z'(2\alpha_y-\alpha_{yz})}{2\sigma_y\sigma_z}\right\}, \tag{17}$$

$$G_x^s = +\frac{f_b\sigma_x'}{{\beta_0}^2{\gamma_0}^3\Lambda_x}\frac{\alpha_x}{\sigma_x\sigma_z}-\frac{f_b\sigma_x'}{2\gamma_0\Lambda_x}\left\{3\frac{3{\Lambda_x}^2\alpha_x-{\sigma_x'}^2\alpha_{xx}}{\sigma_x\sigma_z}+\frac{8{\Lambda_y}^2\alpha_x-{\sigma_y'}^2\alpha_{xy}}{8\sigma_x\sigma_z}+(1-{p_0}^2)\frac{2{\Lambda_z}^2\alpha_x-{\sigma'}^2{}_z\alpha_{xz}}{2\sigma_x\sigma_z}\right\}$$
$$-\frac{f_b\sigma_y'}{8\gamma_0\Lambda_x}\left\{\frac{8{\Lambda_x}^2\alpha_y-{\sigma_x'}^2\alpha_{xy}}{\sigma_y\sigma_z}\right\}-\frac{f_b\sigma_z'}{2\gamma_0\Lambda_x}\left\{(1-{p_0}^2)\frac{2{\gamma_0}^2{\sigma_z}^2{\Lambda_x}^2\alpha_z-{\sigma_x'}^2\sigma_x\sigma_y\alpha_{xz}}{\sigma_x\sigma_y{\gamma_0}^2{\sigma_z}^2}\right\}, \tag{18}$$

$$G_y^s = +\frac{f_b\sigma_y'}{{\beta_0}^2\gamma_0^3\Lambda_y}\frac{\alpha_y}{\sigma_y\sigma_z} - \frac{f_b\sigma_y'}{2\gamma_0\Lambda_y}\left\{3\frac{3{\Lambda_y}^2\alpha_y - \sigma_y'^2\alpha_{yy}}{\sigma_y\sigma_z} + \frac{8{\Lambda_x}^2\alpha_y - \sigma_x'^2\alpha_{xy}}{8\sigma_y\sigma_z} + (1-{p_0}^2)\frac{2{\Lambda_z}^2\alpha_y - \sigma_z'^2\alpha_{yz}}{2\sigma_y\sigma_z}\right\}$$
$$- \frac{f_b\sigma_x'}{8\gamma_0\Lambda_y}\left\{\frac{8{\Lambda_y}^2\alpha_x - \sigma_y'^2\alpha_{xy}}{\sigma_x\sigma_z}\right\} - \frac{f_b\sigma_z'}{2\gamma_0\Lambda_y}\left\{(1-{p_0}^2)\frac{2{\gamma_0}^2{\sigma_z}^2{\Lambda_y}^2\alpha_z - {\sigma_y}'^2\sigma_y\sigma_x\alpha_{yz}}{\sigma_y\sigma_x{\gamma_0}^2{\sigma_z}^2}\right\}, \tag{19}$$

$$G_z^s = +\frac{f_b\sigma_z'}{{\beta_0}^2\gamma_0^3\Lambda_z}\times\frac{\alpha_z}{\sigma_x\sigma_y} - \frac{f_b\sigma_z'}{2\gamma_0\Lambda_z}\left\{3(1-{p_0}^2)\frac{6{\Lambda_z}^2\alpha_z - \sigma'^2{}_z\alpha_{zz}}{2\sigma_x\sigma_y} + \frac{2{\gamma_0}^2{\sigma_z}^2{\Lambda_x}^2\alpha_z - \sigma_x'^2\sigma_x\sigma_y\alpha_{xz}}{2\sigma_x\sigma_y{\gamma_0}^2{\sigma_z}^2}\right.$$
$$\left. + \frac{2{\gamma_0}^2{\sigma_z}^2{\Lambda_y}^2\alpha_z - \sigma_y'^2\sigma_x\sigma_y\alpha_{yz}}{2\sigma_x\sigma_y{\gamma_0}^2{\sigma_z}^2}\right\} - \frac{f_b\sigma_x'}{2\gamma_0\Lambda_z}\left\{\frac{2{\Lambda_z}^2\alpha_x - \sigma'^2{}_z\alpha_{xz}}{\sigma_x\sigma_z}\right\} - \frac{f_b\sigma_y'}{2\gamma_0\Lambda_z}\left\{\frac{2{\Lambda_z}^2\alpha_y - \sigma'^2{}_z\alpha_{yz}}{\sigma_y\sigma_z}\right\}. \tag{20}$$

All space-charge force components in Eqs. (15)–(20) are directly proportional to the $f_b = \eta q_b/8\pi\sqrt{\pi}\epsilon_0$ parameter. Parameter $f_b$ is the only factor that contains the bunch charge. Thus, all the space-charge forces will be scaled up linearly by the total charge of the bunch.

The $\alpha$ parameters are identified as the space-charge enhancement factors, and we call them space-charge coefficients, which are defined as

$$\alpha_x = \int_0^{+\infty}\frac{{k_x}^2 sds}{\sqrt{(u^2+{k_x}^2)^3(u^2+{k_y}^2)(u^2+1)}}, \tag{21}$$

$$\alpha_y = \int_0^{+\infty}\frac{{k_y}^2 sds}{\sqrt{(s^2+{k_x}^2)(s^2+{k_y}^2)^3(s^2+1)}}, \tag{22}$$

$$\alpha_z = \int_0^{+\infty}\frac{k_x k_y sds}{\sqrt{(s^2+{k_x}^2)(s^2+{k_y}^2)(s^2+1)^3}}, \tag{23}$$

$$\alpha_{xx} = \int_0^{+\infty}\frac{3{k_x}^4 sds}{2\sqrt{(s^2+{k_x}^2)^5(s^2+{k_y}^2)(s^2+1)}}, \tag{24}$$

$$\alpha_{yy} = \int_0^{+\infty}\frac{3{k_y}^4 sds}{2\sqrt{(s^2+{k_x}^2)(s^2+{k_y}^2)^5(s^2+1)}}, \tag{25}$$

$$\alpha_{zz} = \int_0^{+\infty}\frac{3k_x k_y sds}{\sqrt{(s^2+{k_x}^2)(s^2+{k_y}^2)(s^2+1)^5}}, \tag{26}$$

$$\alpha_{xy} = \int_0^{+\infty}\frac{4{k_x}^2{k_y}^2 sds}{\sqrt{(s^2+{k_x}^2)^3(s^2+{k_y}^2)^3(s^2+1)}}, \tag{27}$$

$$\alpha_{xz} = \int_0^{+\infty}\frac{{k_x}^2 sds}{\sqrt{(s^2+{k_x}^2)^3(s^2+{k_y}^2)(s^2+1)^3}}, \tag{28}$$

$$\alpha_{yz} = \int_0^{+\infty}\frac{{k_y}^2 sds}{\sqrt{(s^2+{k_x}^2)(s^2+{k_y}^2)^3(s^2+1)^3}}, \tag{29}$$

where $k_x = \sigma_x/\gamma_0\sigma_z$ and $k_y = \sigma_y/\gamma_0\sigma_z$ represent the beam-length ratios in the beam's center-of-mass observer. The space-charge behavior is identified by the ratio between the bunch dimensions in the beam's center-of-mass frame and not the lab frame. The space-charge coefficients take values between zero and one. All space-charge coefficients can be solved numerically. The $\alpha$ coefficients are shown in Fig. 1 for different values of $k_x$ and $k_y$. Note that only three of the $\alpha$ coefficients are independent. For the rest of them, we have $\alpha_x(k_x,k_y) = \alpha_y(k_y,k_x)$, $\alpha_{xx}(k_x,k_y) = \alpha_{yy}(k_y,k_x)$, and $\alpha_{xz}(k_x,k_y) = \alpha_{yz}(k_y,k_x)$. Figure 1 shows that, for very small values of $\sqrt{{k_x}^2+{k_y}^2}$, $\alpha_z$ vanishes, while $\alpha_x$ and $\alpha_y$ both tend to 0.5. This means the bunch looks like a pencil ($\sigma_z \gg \sigma_{x,y}$); thus, the longitudinal space-charge forces can be neglected. In addition, if $k_x$ or $k_y$ are very small, then the $\alpha_z$ coefficient also vanishes, and the beam becomes a sheet in the $x$-$z$ or $y$-$z$ plane. When $\sqrt{{k_x}^2+{k_y}^2}$ tends to very large values, the bunch gets a disk shape in the $x$-$y$ plane and $\alpha_z$ goes to unity, while $\alpha_x$ and $\alpha_y$ both become zero. In this case, the perpendicular components of space-charge forces are negligible in comparison with the longitudinal component.

To solve the envelope equations [Eqs. (3) and (7)] faster, we provide a data table library of $\alpha$ for different values of $k_x$ and $k_y$. Then, all that is required for calculating space-charge forces will be to pick the $\alpha$ coefficients by applying a simple interpolation between the table values [30]. Using this technical trick helps to reduce the necessary time for calculations incredibly because it suppresses the time-consuming process of averaging the space-charge fields over the distribution of the particles in each time

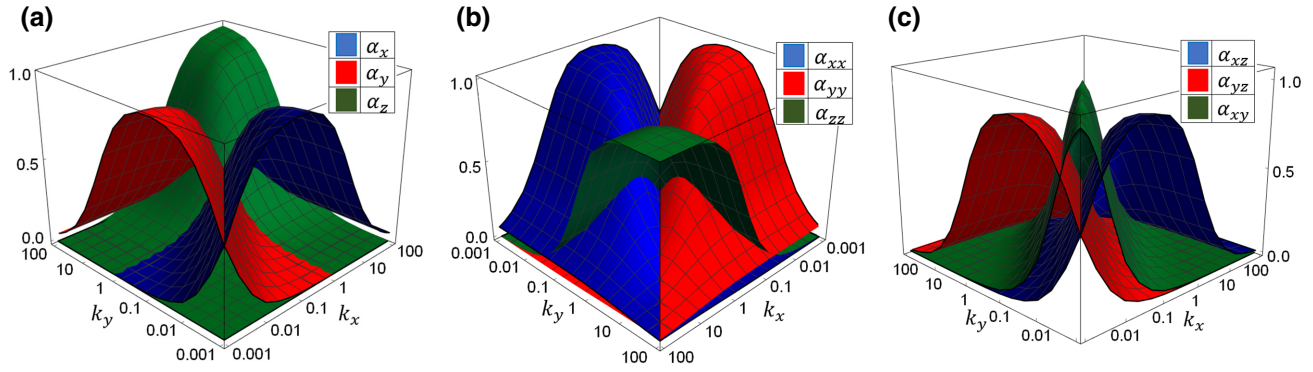


FIG. 1. Space-charge coefficients (a) $\alpha_x$, $\alpha_y$, and $\alpha_z$; (b) $\alpha_{xx}$, $\alpha_{yy}$, and $\alpha_{zz}$; and (c) $\alpha_{xz}$, $\alpha_{yz}$, and $\alpha_{xy}$, in terms of $k_x = \sigma_x/\gamma_0\sigma_z$ and $k_y = \sigma_y/\gamma_0\sigma_z$.

step. Equation (12) shows that each one of the electric field components is an odd function in its own direction and an even function in the other two directions. Therefore, the second- and third-order perturbation terms vanish in $F$-type and $G$-type forces, respectively. There is also coupling between different directions due to $\alpha_{xy}$, $\alpha_{xy}$, and $\alpha_{yz}$ which appears in higher-order perturbation. To validate the presented model, we compare our analytical results with a PIC simulation code (ASTRA) for an asymmetric electron bunch with rms size $\sigma_x = \sqrt{2}$ mm, $\sigma_y = 2\sqrt{2}$ mm, and $\sigma_z = 0.030$ mm; 1% initial energy spread; and initial normalized emittance $\varepsilon_{nx} = 0.05$ μm, $\varepsilon_{ny} = 0.10$ μm, and $\varepsilon_{nz} = 2.93$ μm, which is propagating in a drift section under the influence of its space-charge force. The beam charge is 1 nC with 5 MeV average kinetic energy. The value for $\chi_\tau$ is about $1.7 \times 10^6$, which is a highly space-charge dominated beam and subscript $\tau$ stands for the transverse direction. Figure 2 shows variations in beam size and its divergence along a drift section. The dotted lines and solid lines show the simulations and our analytical results, respectively. The analytical approach has very good consistency with simulations. The reason for the observed insignificant difference in Fig. 2(b) is that the effect of energy spread is only considered in space-charge forces and not in the calculation of space-charge fields.

To benchmark the speed of our presented method, we measure the time required to perform similar calculations with ASTRA for different cell numbers, and the results are compared with the exact particle-tracking codes (Fig. 3). The simulations show that the increase in cell numbers may lead to a reduction in errors in $\sigma_x$ calculations, as the blue line in Fig. 3 shows an error of less than 2% for $32 \times 32 \times 32$ cell numbers. However, the increase in cell numbers makes the calculations excessively costly, so it takes more than a few hours to find the exact results. The analytical calculations take less than 1 s on the same computational resource to do the calculations with the same accuracy. This is what makes the method a practical tool for online accelerator modeling.

Figure 4 verifies that a Gaussian beam is a proper assumption for calculating space-charge fields for all practical beams. In Fig. 4, we consider a non-Gaussian beam with the same parameters as in Fig. 2, although the beam structure is a uniform ellipsoidal distribution in $x$, $y$, and $z$; a uniform elliptical distribution in $p_x p_y$; and a uniform distribution in $p_z$. Comparing Figs. 4 and 2 shows that a Gaussian distribution can estimate the temporal evolution of the beam, even for non-Gaussian distributions, very accurately.

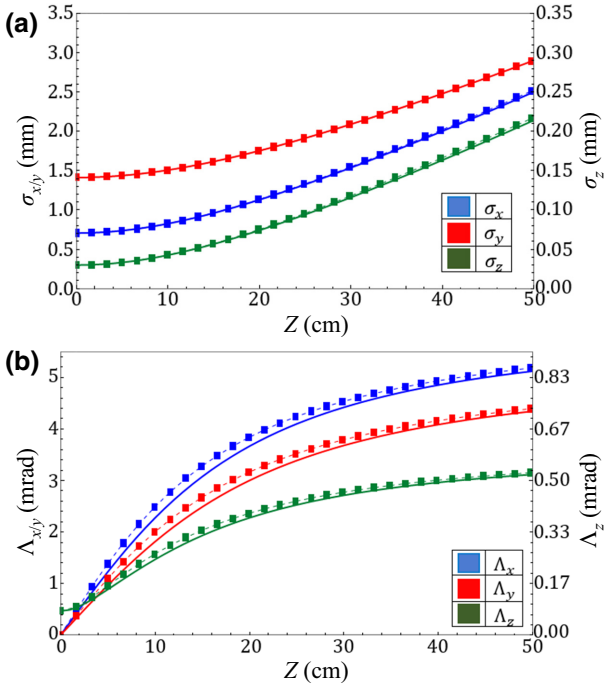


FIG. 2. Variations of (a) bunch size, (b) beam divergence along a drift section due to only space-charge effect. Square dots correspond to simulation results with ASTRA. Solid lines are calculated from the beam-envelope equations.

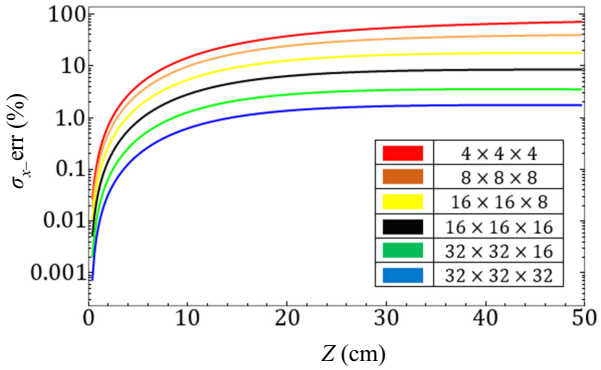


FIG. 3. Assessing the $\sigma_x$ error of the simulation results of ASTRA for different mesh numbers with respect to the exact particle-tracking methods. Number of cells is shown in the inset in the $x$, $y$, and $z$ directions.

Generally, the represented model shows sufficient accuracy, except when the bunch distribution is very different from the Gaussian distribution, e.g., a bunch with a large tail and small head in low energies or a bunch with unresolvable coupling between different directions. To address such cases, more complicated distributions have to be considered. For instance, in the case of asymmetry between the tail and head, a combination of two different Gaussian distributions might be helpful, or in the case of the presence of unresolvable coupling between different directions, the 6D Gaussian distribution can be modified by adding terms representing such couplings. All of these issues will be studied in our future works.

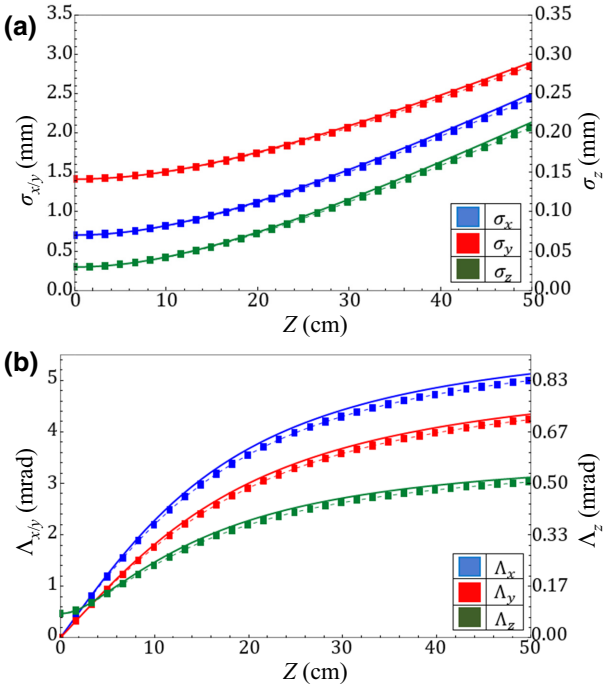


FIG. 4. Variations of (a) bunch size, (b) beam divergence along a drift section due to only the space-charge effect. Square dots correspond to simulation results with ASTRA considering a 6D spheroidal bunch with the same parameters as those used in Fig. 2. Solid lines are calculated from the beam-envelope equations.

## IV. EXTERNAL FORCES

Characterization of the bunch response to accelerator input parameters is often the first step in the accurate modeling of accelerators. In the following section, a variety of external fields applied to a beam in a linear accelerator are considered and the external forces [Eqs. (4) and (8)] in envelope equations are obtained analytically. For comparative purposes, the envelope equations are solved and the results are benchmarked against the simulation outcome.

### A. Solenoidal magnets

Solenoid magnets are extensively used to transport low-energy beams (up to a few hundred MeV) in an accelerator line and have a negligible destructive effect on beam quality [31,32]. The solenoid magnetic field is very linear and up to the first order with respect to $\Delta x$, $\Delta y$, and $\Delta z$ [32,33]:

$$\vec{B}^{\mathrm{SM}} = (\mu^{\mathrm{SM}} + \Delta z \mu_z^{\mathrm{SM}})\hat{z} - \frac{\Delta x}{2}\mu_z^{\mathrm{SM}}\hat{x} - \frac{\Delta y}{2}\mu_z^{\mathrm{SM}}\hat{y}, \quad (30)$$

where $\mu^{\mathrm{SM}} = (\vec{B}^{\mathrm{SM}} \cdot \hat{z})|^{\Delta\vec{r}=0}$ and $\mu_z^{\mathrm{SM}} = ((\partial/\partial z)\vec{B}^{\mathrm{SM}} \cdot \hat{z})|^{\Delta\vec{r}=0}$ are the on-axis magnetic field of the solenoid and its first derivative with respect to $z_0$, respectively. Substituting the solenoid magnetic field in Eqs. (4) and (8), the generalized external-force components to the third-order perturbation are

$$\begin{aligned} F_x^e = &-\frac{\eta^2 c^2}{4{p_0}^2}\left(\mu^{\mathrm{SM}\,2} + \mu_z^{\mathrm{SM}\,2}{\sigma_z}^2\right)\sigma_x + \eta^2 c^2 \mu^{\mathrm{SM}}\mu_z^{\mathrm{SM}}\sigma_x\sigma_z\sigma_z' \\ &+ \frac{\eta^2 c^2 \mu^{\mathrm{SM}\,2}}{4}\sigma_x\left(2{\sigma_x'}^2 + {\Lambda_x}^2 + {\Lambda_y}^2 + {\Lambda_z}^2\right) \\ &+ \frac{\eta^2 c^2 \mu_z^{\mathrm{SM}\,2}}{4}\sigma_x{\sigma_z}^2\left(2{\sigma_x'}^2 + 2{\sigma'}^2{}_z + {\Lambda_x}^2\right. \\ &\left. + {\Lambda_y}^2 + {\Lambda_z}^2\right), \end{aligned} \quad (31)$$

$$\begin{aligned} F_y^e = &-\frac{\eta^2 c^2}{4{p_0}^2}\left(\mu^{\mathrm{SM}\,2} + \mu_z^{\mathrm{SM}^2}{\sigma_z}^2\right)\sigma_y + \eta^2 c^2 \mu^{\mathrm{SM}}\mu_z^{\mathrm{SM}}\sigma_y\sigma_z\sigma_z' \\ &+ \frac{\eta^2 c^2 \mu^{\mathrm{SM}^2}}{4}\sigma_y\left(2{\sigma_y'}^2 + {\Lambda_y}^2 + {\Lambda_x}^2 + {\Lambda_z}^2\right) \\ &+ \frac{\eta^2 c^2 \mu_z^{\mathrm{SM}^2}}{4}\sigma_y{\sigma_z}^2\left(2{\sigma_y'}^2 + 2{\sigma'}^2{}_z + {\Lambda_y}^2\right. \\ &\left. + {\Lambda_x}^2 + {\Lambda_z}^2\right), \end{aligned} \quad (32)$$

$$F_z^e = 0, \quad (33)$$

$$G_x^e = -\frac{\eta^2 c^2}{4{p_0}^2 \Lambda_x}(\mu^{\mathrm{SM}^2} + \mu_z^{\mathrm{SM}^2}{\sigma_z}^2)\sigma_x\sigma_x' + \frac{\eta^2 c^2 \mu^{\mathrm{SM}}\mu_z^{\mathrm{SM}}}{\Lambda_x}\sigma_x\sigma_x'\sigma_z\sigma_z' + \frac{\eta^2 c^2 \mu^{\mathrm{SM}^2}}{4\Lambda_x}\sigma_x\sigma_x'\left(3{\Lambda_x}^2 - {\Lambda_y}^2 - {\Lambda_z}^2\right) + \frac{\eta^2 c^2 \mu_z^{\mathrm{SM}^2}}{4\Lambda_x}\sigma_x\sigma_x'{\sigma_z}^2\left(2{\sigma'}^2{}_z + 3{\Lambda_x}^2 + {\Lambda_y}^2 + {\Lambda_z}^2\right), \tag{34}$$

$$G_y^e = -\frac{\eta^2 c^2}{4{p_0}^2 \Lambda_y}\left(\mu^{\mathrm{SM}^2} + \mu_z^{\mathrm{SM}^2}{\sigma_z}^2\right)\sigma_y\sigma_y' + \frac{\eta^2 c^2 \mu^{\mathrm{SM}}\mu_z^{\mathrm{SM}}}{\Lambda_y}\sigma_y\sigma_y'\sigma_z\sigma_z' + \frac{\eta^2 c^2 \mu^{\mathrm{SM}^2}}{4\Lambda_y}\sigma_y\sigma_y'\left(3{\Lambda_y}^2 - {\Lambda_x}^2 - {\Lambda_z}^2\right) + \frac{\eta^2 c^2 \mu_z^{\mathrm{SM}^2}}{4\Lambda_y}\sigma_y\sigma_y'{\sigma_z}^2\left(2{\sigma'}^2{}_z + 3{\Lambda_y}^2 + {\Lambda_x}^2 + {\Lambda_z}^2\right), \tag{35}$$

$$G_z^e = 0. \tag{36}$$

The longitudinal forces in all orders of perturbation are equal to zero; thus, the bunch length is not affected by the solenoid directly. Since $G_z^e = 0$, the longitudinal divergence, $\Lambda_z$, remains constant [Eq. (7)]. Nonetheless, $\sigma_z$ can vary, even for $F_z^e = 0$, because of the emittance-force effect (in the absence of space-charge forces) in this direction.

The solenoidal forces are linearly proportional to $\sigma_u$ and $\sigma_u\sigma_u'/\Lambda_u$, respectively, for $F$ and $G$ types in the corresponding direction. In the lowest order, the effect of the solenoid on the beam is quadratically proportional to $(\eta/p_0)\sqrt{\mu^{\mathrm{SM}^2} + \mu_z^{\mathrm{SM}^2}{\sigma_z}^2}$, which means that the solenoid force is independent of the charge sign. It is such that the $F$-type forces are purely focusing and the $G$-type forces, depending on the sign of $\sigma_u'$, can be focusing or defocusing.

The higher orders of perturbation include both focusing and defusing terms simultaneously. Thus, not only is the field profile, $\mu^{\mathrm{SM}}$ ,determinative, but its derivate, $\mu_z^{\mathrm{SM}}$, also plays an important role in the effect of the field on the beam. Here, the charge sign must also be considered and correlations between the different directions also appear, which is not the case in the previous order.

To compare simulations with ASTRA and our analytical method, a long solenoid applies a field of $\mu^{\mathrm{SM}}(z) = 0.5\,z$ to the bunch, as already considered in Sec. III. Figure 5 shows that the simulation and analytical data are in very good agreement.

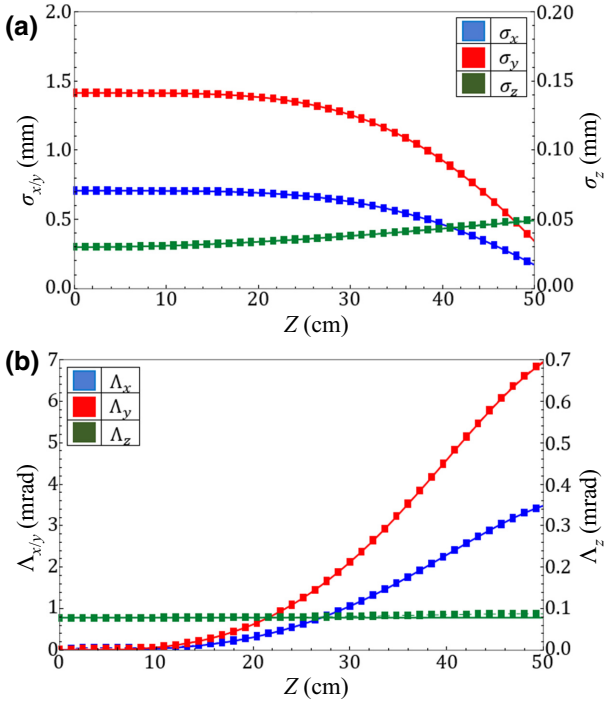


FIG. 5. Variations of bunch envelopes (a) bunch size, (b) beam divergence along a solenoid. Square dots correspond to simulation results with ASTRA. Solid lines are calculated from the beam-envelope equations.

### B. Electrostatic lenses

Electrostatic lenses are employed for focusing (defocusing) and accelerating (decelerating) beams of low-energy electrons and ions [34,35]. The most widely used application of such lenses is the first acceleration of electrons in thermionic electron guns, where the particles initiate at a hot cathode with a fraction of eV energy [36,37]. Then using a convenient geometry and induced potentials for the positive and negative electrodes, the emitted electrons form a beam of the required energy and quality [38,39]. The corresponding electric field is largely linear and up to first order with respect to $\Delta x$, $\Delta y$, and $\Delta z$ [14]:

$$\vec{E}^{\mathrm{el}} = (\varepsilon^{\mathrm{el}} + \Delta z\varepsilon_z^{\mathrm{el}})\hat{z} - \frac{\Delta x}{2}\varepsilon_z^{\mathrm{el}}\hat{x} - \frac{\Delta y}{2}\varepsilon_z^{\mathrm{el}}\hat{y}, \tag{37}$$

where $\varepsilon^{\mathrm{el}} = (\vec{E}^{\mathrm{el}}\cdot\hat{z})|^{\Delta\vec{r}=0}$ and $\mathcal{E}_z^{\mathrm{el}} = ((\partial/\partial z)\vec{E}^{\mathrm{el}}\cdot\hat{z})|^{\Delta\vec{r}=0}$ represent the on-axis electric field of the lens and its first derivative with respect to $z$ at the location of the reference particle, respectively. Substituting Eq. (37) into Eqs. (4) and (8), the generalized external-force components to the third-order perturbation are

$$F_x^e = -\frac{\eta\varepsilon_z^{\rm el}}{2\gamma_0{\beta_0}^2}\sigma_x - \frac{\eta\varepsilon^{\rm el}}{\gamma_0}\sigma_x' + \frac{\eta\varepsilon_z^{\rm el}}{4\gamma_0}\Big\{2\sigma_y\sigma_y'\sigma_x' - 4(1-{p_0}^2)\sigma_z\sigma_z'\sigma_x' + {\gamma_0}^4{\Lambda_z}^2\sigma_x + 2(2+{\gamma_0}^2)\sigma_x{\sigma_x'}^2$$
$$+ (2+{\gamma_0}^2){\Lambda_x}^2\sigma_x + {\gamma_0}^2{\Lambda_y}^2\sigma_x\Big\} + \frac{\eta\varepsilon^{\rm el}{p_0}^2}{2\gamma_0}\sigma_x'\left\{(2+{\gamma_0}^2){\Lambda_z}^2 + 3{\Lambda_x}^2 + {\Lambda_y}^2\right\}, \tag{38}$$

$$F_y^e = -\frac{\eta\varepsilon_z^{\rm el}}{2\gamma_0{\beta_0}^2}\sigma_y - \frac{\eta\varepsilon^{\rm el}}{\gamma_0}\sigma_y' + \frac{\eta\varepsilon_z^{\rm el}}{4\gamma_0}\Big\{2\sigma_x\sigma_x'\sigma_y' - 4(1-{p_0}^2)\sigma_z\sigma_z'\sigma_y' + {\gamma_0}^4{\Lambda_z}^2\sigma_y + 2(2+{\gamma_0}^2)\sigma_y{\sigma_y'}^2$$
$$+ (2+{\gamma_0}^2){\Lambda_y}^2\sigma_y + {\gamma_0}^2{\Lambda_x}^2\sigma_y\Big\} + \frac{\eta\varepsilon^{\rm el}{p_0}^2}{2\gamma_0}\sigma_y'\left\{(2+{\gamma_0}^2){\Lambda_z}^2 + 3{\Lambda_y}^2 + {\Lambda_x}^2\right\}, \tag{39}$$

$$F_z^e = \frac{\eta\varepsilon_z^{\rm el}}{\gamma_0{p_0}^2}\sigma_z - \frac{3\eta\varepsilon^{\rm el}}{\gamma_0}\sigma_z' + \frac{\eta\varepsilon_z^{\rm el}}{2\gamma_0}\Big\{(1-{p_0}^2)(\sigma_x\sigma_x' + \sigma_y\sigma_y')\sigma_z' + (6-3{\gamma_0}^2-2{\gamma_0}^4)(2{\sigma'}^2{}_z + {\Lambda_z}^2)\sigma_z - ({\Lambda_x}^2+{\Lambda_y}^2)\sigma_z\Big\}$$
$$+ \frac{\eta\varepsilon^{\rm el}{p_0}^2}{2\gamma_0}\sigma_z'\left\{3(2+{\gamma_0}^2){\Lambda_z}^2 + ({\Lambda_x}^2+{\Lambda_y}^2)\right\}, \tag{40}$$

$$G_x^e = -\frac{\eta\varepsilon_z^{\rm el}}{2\gamma_0{\beta_0}^2\Lambda_x}\sigma_x\sigma_x' - \frac{\eta\varepsilon^{\rm el}}{\gamma_0}\Lambda_x$$
$$+ \frac{\eta\varepsilon_z^{\rm el}}{4\Lambda_x\gamma_0}\Big\{6{\Lambda_x}^2\sigma_x\sigma_x' + 2{\Lambda_x}^2\sigma_y\sigma_y' - 4(1-{p_0}^2){\Lambda_x}^2\sigma_z\sigma_z' + {\gamma_0}^2\sigma_x\sigma_x'({\gamma_0}^2{\Lambda_z}^2 + 3{\Lambda_x}^2 + {\Lambda_y}^2)\Big\}, \tag{41}$$

$$G_y^e = -\frac{\eta\varepsilon_z^{\rm el}}{2\gamma_0{\beta_0}^2\Lambda_x}\sigma_y\sigma_y' - \frac{\eta\varepsilon^{\rm el}}{\gamma_0}\Lambda_y$$
$$+ \frac{\eta\varepsilon_z^{\rm el}}{4\Lambda_y\gamma_0}\Big\{6{\Lambda_y}^2\sigma_y\sigma_y' + 2{\Lambda_y}^2\sigma_x\sigma_x' - 4(1-{p_0}^2){\Lambda_y}^2\sigma_z\sigma_z' + {\gamma_0}^2\sigma_y\sigma_y'({\gamma_0}^2{\Lambda_z}^2 + 3{\Lambda_y}^2 + {\Lambda_x}^2)\Big\}, \tag{42}$$

$$G_z^e = +\frac{\eta\varepsilon_z^{\rm el}}{\gamma_0{p_0}^2\Lambda_z}\sigma_z\sigma_z' - \frac{3\eta\varepsilon^{\rm el}}{\gamma_0}\Lambda_z$$
$$+ \frac{\eta\varepsilon_z^{\rm el}}{2\gamma_0\Lambda_z}\Big\{3(6-3{\gamma_0}^2-2{\gamma_0}^4){\Lambda_z}^2\sigma_z\sigma_z' - ({\Lambda_x}^2+{\Lambda_y}^2)\sigma_z\sigma_z' + (1-{p_0}^2)(\sigma_x\sigma_x' + \sigma_y\sigma_y'){\Lambda_z}^2\Big\}. \tag{43}$$

In the lowest order, the signs of $\eta\mathcal{E}_z^{\rm el}$ and $\eta\mathcal{E}_z^{\rm el}\sigma_u'$ indicate whether the force is focusing or defocusing for $F$- and $G$-type forces, respectively. Therefore, focusing the bunch length in the longitudinal direction leads to defocusing in the transverse plane and vice versa. Note that the longitudinal forces even appear in the lowest order of perturbation in electrostatic lenses, unlike the solenoidal magnets. On the other hand, similar to the solenoidal forces, the electrostatic forces are linearly proportional to $\sigma_u$ and $\sigma_u\sigma_u'/\Lambda_u$, respectively, for $F$ and $G$ types in the corresponding direction. In the next order, all forces are similarly proportional to the value of the electric field on the beam axis, $\varepsilon^{\rm el}$. The slope of the electric field on the beam axis defines the force behavior for the highest-order term.

To compare the results of our analytical model against simulations, an electrostatic lens with a field defined by $\varepsilon^{\rm el}(z) = 6\times10^6\, z$ and an electron beam with the same parameters as those reported in Sec. III, except with an average energy of 1 keV and longitudinal emittance of 0.01 μm, are considered. The results of ASTRA simulations and analytical calculations are shown in Fig. 6. The dotted lines and solid lines show the simulations and our analytical results, respectively. Analytical estimates for the beam's general parameters are in excellent agreement with numerical results.

### C. Quadrupole magnets

Quadrupole magnets provide strong focusing fields and are frequently used to transport high-energy beams along the accelerator line [40,41]. Quadrupoles focus only in one plane and defocus in the other one, and then asymmetric forces are applied to the beam. The magnetic fields of the quadrupoles have the following mathematical form [42]:

$$\overrightarrow{B^{\rm QM}} = \frac{p_0 k^{\rm QM}}{\eta c}(\Delta y\hat{x} + \Delta x\hat{y}), \tag{44}$$

where $k^{\rm QM}$ indicates the well-known characteristic of the quadrupole magnet, i.e., the quadrupole strength. Substituting Eq. (44) into Eqs. (4) and (8), the generalized external-force components to the third-order perturbation are

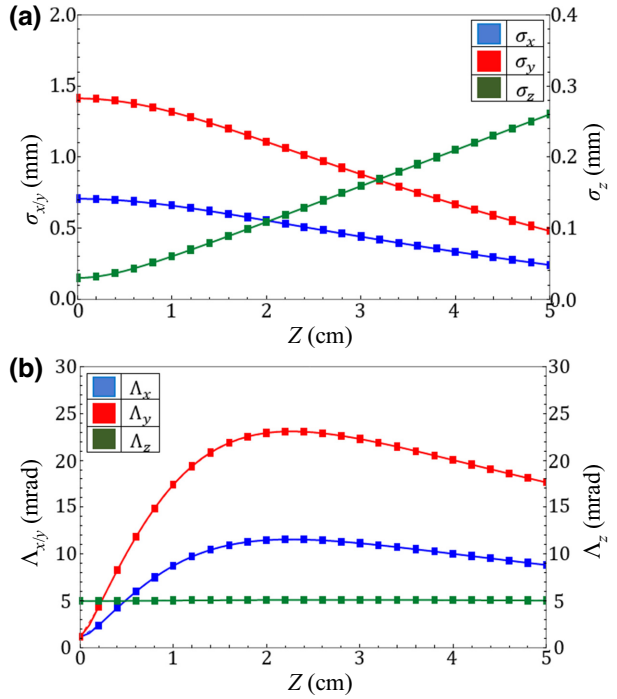


FIG. 6. Variations of (a) bunch size, (b) beam divergence along an electrostatic lens. Square dots correspond to simulation results with ASTRA. Solid lines are calculated from the beam-envelope equations.

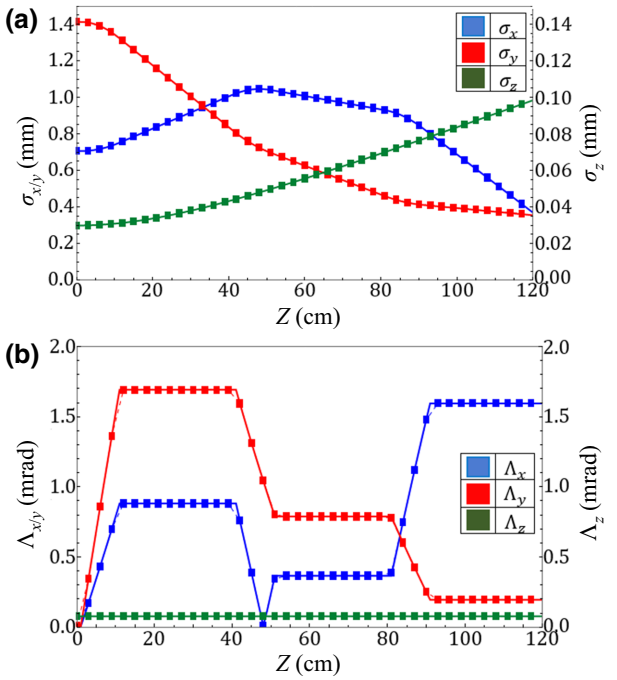


FIG. 7. Variations of bunch envelopes (a) bunch size, (b) beam divergence along a triplet set of quadrupole magnets. Square dots correspond to simulation results with ASTRA. Solid lines are calculated from the beam-envelope equations.

$$F_x^e = -k^{\mathrm{QM}}\sigma_x + \frac{k^{\mathrm{QM}}{p_0}^2}{2}\sigma_x \times \left\{(2+{\gamma_0}^2){\Lambda_z}^2 + 2{\sigma_x'}^2 + {\Lambda_x}^2 + {\Lambda_y}^2\right\}, \tag{45}$$

$$F_y^e = +k^{\mathrm{QM}}\sigma_y - \frac{k^{\mathrm{QM}}{p_0}^2}{2}\sigma_y \left\{(2+{\gamma_0}^2){\Lambda_z}^2 + 2{\sigma_y'}^2 + {\Lambda_y}^2 + {\Lambda_x}^2\right\}, \tag{46}$$

$$F_z^e = -k^{\mathrm{QM}}{p_0}^2\sigma_z'(\sigma_x\sigma_x' - \sigma_y\sigma_y'), \tag{47}$$

$$G_x^e = -\frac{k^{\mathrm{QM}}}{\Lambda_x}\sigma_x\sigma_x' + \frac{k^{\mathrm{QM}}{p_0}^2}{2\Lambda_x}\sigma_x\sigma_x' \left\{(2+{\gamma_0}^2){\Lambda_z}^2 + 3{\Lambda_x}^2 + {\Lambda_y}^2\right\}, \tag{48}$$

$$G_y^e = +\frac{k^{\mathrm{QM}}}{\Lambda_y}\sigma_y\sigma_y' - \frac{k^{\mathrm{QM}}{p_0}^2}{2\Lambda_y}\sigma_y\sigma_y' \left\{(2+{\gamma_0}^2){\Lambda_z}^2 + 3{\Lambda_y}^2 + {\Lambda_x}^2\right\}, \tag{49}$$

$$G_z^e = -k^{\mathrm{QM}}{p_0}^2\Lambda_z(\sigma_x\sigma_x' - \sigma_y\sigma_y'). \tag{50}$$

The effect of the quadrupoles in all orders is directly proportional to $k^{\mathrm{QM}}$. Only the second- and third-order perturbations appear in longitudinal $F$-type and $G$-type forces, respectively. Asymmetric variations in the transversal beam sizes cause the bunch length and divergence to change. In the lowest order, the sign of $k^{\mathrm{QM}}$ reveals that the focusing effect on $\sigma_x$ and $\sigma_y$ is opposite. Interestingly, for $F_x^e$ and $F_y^e$, the second-order terms oppose the first order. The transversal $G$-type forces act like those of $F$ type, except the forces are also directly proportional to $\sigma_u'$ for the related direction. Figure 7 shows the effect of a triplet set of quadrupole magnets with specifications defined in Table I for the bunch of electrons considered in Sec. III.

### D. Radio-frequency forces

A radio-frequency (rf) cavity is used to accelerate or decelerate a bunch of charged particles or even manipulate its phase space through energy transformation between the

TABLE I. Quadrupole specifications for the fourth example. $L$ and $z$ indicate the length and location of a quadrupole center, respectively.

| Element | $k^{\mathrm{QM}}$ (1/m$^2$) | $L$ (cm) | $z$ (cm) |
|---|---|---|---|
| $Q_1$ | −12.221 | 10 | 6.0 |
| $Q_2$ | +12.018 | 10 | 46 |
| $Q_3$ | +13.776 | 10 | 86 |

excited fields in the cavity and the passing particles in conventional accelerators [43,44].

The electromagnetic fields in a rf cavity are [45]

$$\vec{E}^{\mathrm{rf}} = (\mathcal{E}^{\mathrm{rf}} + \Delta z \mathcal{E}_z^{\mathrm{rf}})\hat{z} - \frac{\Delta x}{2}\mathcal{E}_z^{\mathrm{rf}}\hat{x} - \frac{\Delta y}{2}\mathcal{E}_z^{\mathrm{rf}}\hat{y}, \tag{51}$$

$$\vec{B}^{\mathrm{rf}} = -\frac{\Delta y}{2c}\mathcal{E}_t^{\mathrm{rf}}\hat{x} + \frac{\Delta x}{2c}\mathcal{E}_t^{\mathrm{rf}}\hat{y}, \tag{52}$$

where $\mathcal{E}^{\mathrm{rf}} = (\vec{E}^{\mathrm{rf}} \cdot \hat{z})|^{\Delta\vec{r}=0}$, $\mathcal{E}_z^{\mathrm{rf}} = ((\partial/\partial z)\vec{E}^{\mathrm{rf}} \cdot \hat{z})|^{\Delta\vec{r}=0}$, and $\mathcal{E}_t^{\mathrm{rf}} = ((\partial/c\partial t)\vec{E}^{\mathrm{rf}} \cdot \hat{z})|^{\Delta\vec{r}=0}$ represent the on-axis electric field of the rf field and its first derivative with respect to $z$ and $t$ at $z_0$, respectively. $\mathcal{E}_z^{\mathrm{rf}}$ and $\mathcal{E}_t^{\mathrm{rf}}$ are proportional to the radial electric field component and azimuthal magnetic field component, respectively. By substituting Eqs. (51) and (52) into Eqs. (4) and (8), the generalized external force of a rf cavity to the third-order perturbation is

$$\begin{aligned}
F_x^e = &-\frac{\eta(\mathcal{E}_z^{\mathrm{rf}} + \beta_0\mathcal{E}_t^{\mathrm{rf}})}{2\gamma_0{\beta_0}^2}\sigma_x - \frac{\eta\mathcal{E}^{\mathrm{rf}}}{\gamma_0}\sigma_x' + \frac{\eta\mathcal{E}_z^{\mathrm{rf}}}{2\gamma_0}\sigma_x'\left\{\sigma_y\sigma_y' - 2(1-{p_0}^2)\sigma_z\sigma_z'\right\} \\
&+ \frac{\eta\mathcal{E}_z^{\mathrm{rf}}}{4\gamma_0}\sigma_x\left\{{\gamma_0}^4{\Lambda_z}^2 + 2(2+{\gamma_0}^2)\sigma_x'^2 + (2+{\gamma_0}^2){\Lambda_x}^2 + {\gamma_0}^2{\Lambda_y}^2\right\} \\
&+ \frac{\eta p_0\mathcal{E}_t^{\mathrm{rf}}}{4}\sigma_x\left\{(2+{\gamma_0}^2){\Lambda_z}^2 + 2\sigma_x'^2 + ({\Lambda_x}^2 + {\Lambda_y}^2)\right\} + \frac{\eta{p_0}^2\mathcal{E}^{\mathrm{rf}}}{2\gamma_0}\sigma_x'\left\{(2+{\gamma_0}^2){\Lambda_z}^2 + 3{\Lambda_x}^2 + {\Lambda_y}^2\right\},
\end{aligned} \tag{53}$$

$$\begin{aligned}
F_y^e = &-\frac{\eta(\mathcal{E}_z^{\mathrm{rf}} + \beta_0\mathcal{E}_t^{\mathrm{rf}})}{2\gamma_0{\beta_0}^2}\sigma_y - \frac{\eta\mathcal{E}^{\mathrm{rf}}}{\gamma_0}\sigma_y' + \frac{\eta\mathcal{E}_z^{\mathrm{rf}}}{2\gamma_0}\sigma_y'\left\{\sigma_x\sigma_x' - 2(1-{p_0}^2)\sigma_z\sigma_z'\right\} \\
&+ \frac{\eta\mathcal{E}_z^{\mathrm{rf}}}{4\gamma_0}\sigma_y\left\{{\gamma_0}^4{\Lambda_z}^2 + 2(2+{\gamma_0}^2)\sigma_y'^2 + (2+{\gamma_0}^2){\Lambda_y}^2 + {\gamma_0}^2{\Lambda_x}^2\right\} \\
&+ \frac{\eta p_0\mathcal{E}_t^{\mathrm{rf}}}{4}\sigma_y\left\{(2+{\gamma_0}^2){\Lambda_z}^2 + 2\sigma_y'^2 + ({\Lambda_y}^2 + {\Lambda_x}^2)\right\} + \frac{\eta{p_0}^2\mathcal{E}^{\mathrm{rf}}}{2\gamma_0}\sigma_y'\left\{(2+{\gamma_0}^2){\Lambda_z}^2 + 3{\Lambda_y}^2 + {\Lambda_x}^2\right\},
\end{aligned} \tag{54}$$

$$\begin{aligned}
F_z^e = &+\frac{\eta\mathcal{E}_z^{\mathrm{rf}}}{\gamma_0{p_0}^2}\sigma_z - \frac{3\eta\mathcal{E}^{\mathrm{rf}}}{\gamma_0}\sigma_z' + \frac{\eta(1-{p_0}^2)\mathcal{E}_z^{\mathrm{rf}}}{2\gamma_0}\sigma_z'(\sigma_x\sigma_x' + \sigma_y\sigma_y') - \frac{\eta p_0\mathcal{E}_t^{\mathrm{rf}}}{2}\sigma_z'(\sigma_x\sigma_x' + \sigma_y\sigma_y') \\
&+ \frac{\eta\mathcal{E}_z^{\mathrm{rf}}}{2\gamma_0}\sigma_z\left\{(6-3{\gamma_0}^2-2{\gamma_0}^4)(2\sigma'^2{}_z + {\Lambda_z}^2) - ({\Lambda_x}^2 + {\Lambda_y}^2)\right\} + \frac{\eta{p_0}^2\mathcal{E}^{\mathrm{rf}}}{2\gamma_0}\sigma_z'\left\{3(2+{\gamma_0}^2){\Lambda_z}^2 + ({\Lambda_x}^2 + {\Lambda_y}^2)\right\},
\end{aligned} \tag{55}$$

$$\begin{aligned}
G_x^e = &-\frac{\eta(\mathcal{E}_z^{\mathrm{rf}} + \beta_0\mathcal{E}_t^{\mathrm{rf}})}{2\gamma_0{\beta_0}^2\Lambda_x}\sigma_x\sigma_x' - \frac{\eta\mathcal{E}^{\mathrm{rf}}}{\gamma_0}\Lambda_x + \frac{\eta\mathcal{E}_z^{\mathrm{rf}}}{2\gamma_0}\Lambda_x\left\{3\sigma_x\sigma_x' + \sigma_y\sigma_y' - 2(1-{p_0}^2)\sigma_z\sigma_z'\right\} \\
&+ \frac{\eta\gamma_0\mathcal{E}_z^{\mathrm{rf}}}{4\Lambda_x}\sigma_x\sigma_x'\left({\gamma_0}^2{\Lambda_z}^2 + 3{\Lambda_x}^2 + {\Lambda_y}^2\right) + \frac{\eta p_0\mathcal{E}_t^{\mathrm{rf}}}{4\Lambda_x}\sigma_x\sigma_x'\left\{(3+{p_0}^2){\Lambda_z}^2 + 3{\Lambda_x}^2 + {\Lambda_y}^2\right\}
\end{aligned} \tag{56}$$

$$\begin{aligned}
G_y^e = &-\frac{\eta(\mathcal{E}_z^{\mathrm{rf}} + \beta_0\mathcal{E}_t^{\mathrm{rf}})}{2\gamma_0{\beta_0}^2\Lambda_y}\sigma_y\sigma_y' - \frac{\eta\mathcal{E}^{\mathrm{rf}}}{\gamma_0}\Lambda_y + \frac{\eta\mathcal{E}_z^{\mathrm{rf}}}{2\gamma_0}\Lambda_y\left\{3\sigma_y\sigma_y' + \sigma_x\sigma_x' - 2(1-{p_0}^2)\sigma_z\sigma_z'\right\} \\
&+ \frac{\eta\gamma_0\mathcal{E}_z^{\mathrm{rf}}}{4\Lambda_y}\sigma_y\sigma_y'\left({\gamma_0}^2{\Lambda_z}^2 + 3{\Lambda_y}^2 + {\Lambda_x}^2\right) + \frac{\eta p_0\mathcal{E}_t^{\mathrm{rf}}}{4\Lambda_y}\sigma_y\sigma_y'\left\{(3+{p_0}^2){\Lambda_z}^2 + 3{\Lambda_y}^2 + {\Lambda_x}^2\right\},
\end{aligned} \tag{57}$$

$$\begin{aligned}
G_z^e = &+\frac{\eta\mathcal{E}_z^{\mathrm{rf}}}{\gamma_0{p_0}^2\Lambda_z}\sigma_z\sigma_z' - \frac{3\eta\mathcal{E}^{\mathrm{rf}}}{\gamma_0}\Lambda_z + \frac{\eta(1-{p_0}^2)\mathcal{E}_z^{\mathrm{rf}}}{2\gamma_0}\Lambda_z\left(\sigma_x\sigma_x' + \sigma_y\sigma_y'\right) - \frac{\eta p_0\mathcal{E}_t^{\mathrm{rf}}}{2}\Lambda_z\left(\sigma_x\sigma_x' + \sigma_y\sigma_y'\right) \\
&+ \frac{\eta\mathcal{E}_z^{\mathrm{rf}}}{2\gamma_0\Lambda_z}\sigma_z\sigma_z'\left\{3(6-3{\gamma_0}^2-2{\gamma_0}^4){\Lambda_z}^2 - ({\Lambda_x}^2 + {\Lambda_y}^2)\right\}.
\end{aligned} \tag{58}$$

The lowest order shows the same features of the electrostatic lenses, except that in the presence of rf magnetic fields the transverse forces are linearly proportional to $\mathcal{E}_z^{\mathrm{rf}} + \beta_0\mathcal{E}_t^{\mathrm{rf}}$ instead of $\mathcal{E}_z^{\mathrm{rf}}$. In a traveling-wave rf cavity, the electric force will cancel out the effect of the magnetic force completely in the transverse plane at high energies.

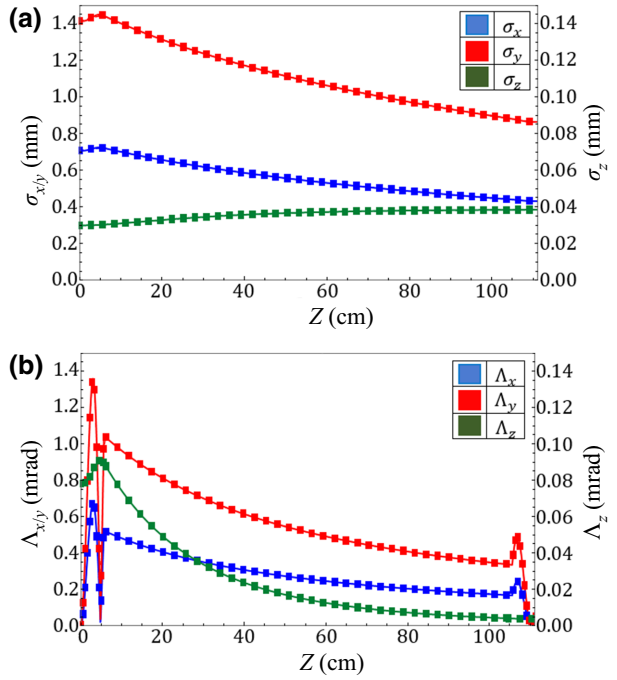


FIG. 8. Variations of bunch envelopes (a) bunch size, (b) beam divergence along an rf cavity. Square dots correspond to simulation results with ASTRA. Solid lines are calculated from the beam-envelope equations.

This is not the case for standing-wave rf structures, where the field dependencies on $t$ and $z$ are independent and there is a $\pi/2$ phase difference between the two radial rf forces. The second nonvanishing order of all forces is proportional to $(\eta\varepsilon^{\mathrm{el}}/\gamma_0)\sigma_u'$ and $(\eta\varepsilon^{\mathrm{el}}/\gamma_0)\Lambda_u$ for $F$ type and $G$ type, respectively. The highest-order term of the forces is the same as the electrostatic lens, except that there is an additional effect due to the presence of the rf magnetic field appearing in the equations as $\mathcal{E}_t^{\mathrm{rf}}$.

Figure 8 shows a comparison between ASTRA simulations and envelope-equation results. The bunch in Sec. III

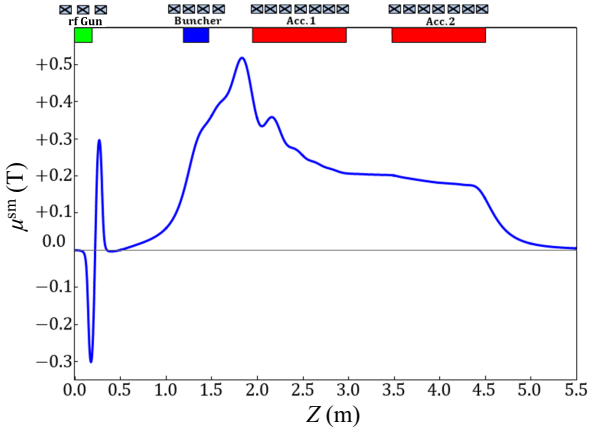


FIG. 10. On-axis magnetic field profile of the designed solenoid for the AWAKE injector.

is considered to pass a standard 31-cell $S$-band (3-GHz) traveling-wave structure with a phase advance of $2\pi/3$ per cell, phase velocity equal to the velocity of light, and 15 MV/m constant gradient. The results represent good consistency.

## V. APPLICATION FOR AWAKE PHOTOINJECTOR

In this section, we apply our investigated analytical approach to the photoinjector of the AWAKE in run 2 [46]. This photoinjector is designed to generate ultrashort ($\sigma_z \cong 60$ μm), high-current ($q_b \cong 100$ pC), and very-high-quality electron bunches ($\varepsilon_{nx} \leq 1$ μm rad) [47]. The general layout of the injector is presented in Fig. 9. The injector starts from a 1.6-cell $S$-band ($\nu = 2998.5$ MHz) rf gun, which is capable of providing a maximum field gradient of 120 MV/m on the cathode. The cathode is located on the left wall of the first cell, where a UV laser illuminates it to generate a 100-pC 1-ps electron beam with a very low intrinsic emittance of about 0.26 mm mrad.

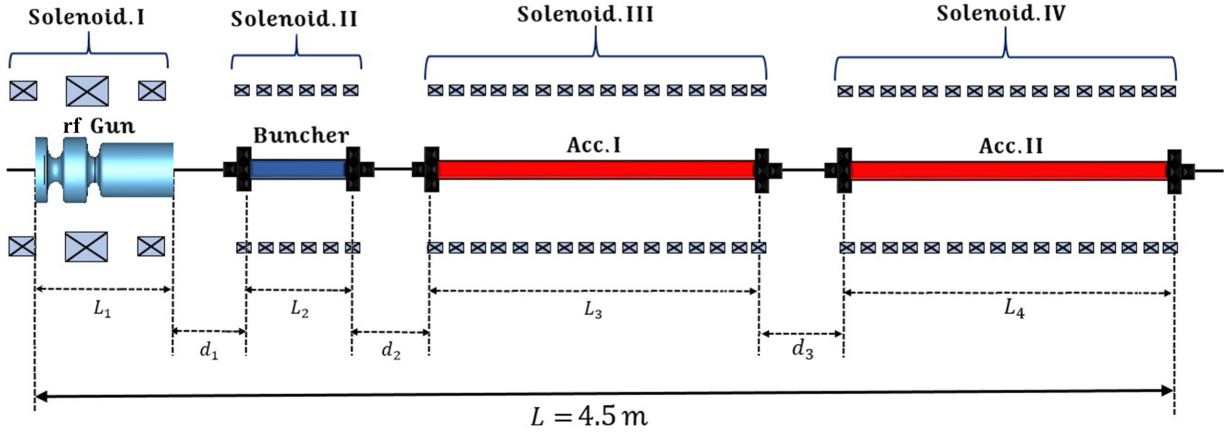


FIG. 9. Layout of the AWAKE injector.

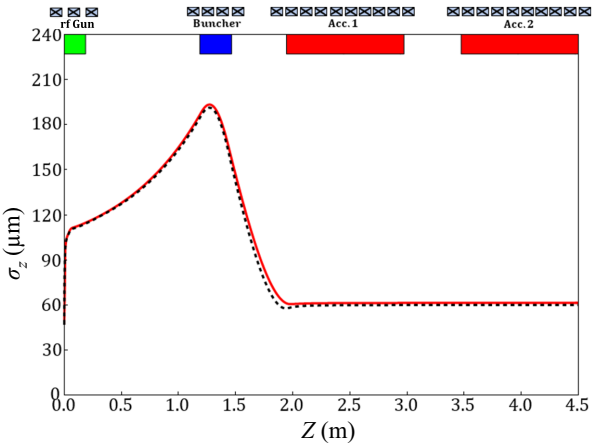


FIG. 11. Variations of the bunch length along the AWAKE photoinjector. Black dots correspond to simulation results with ASTRA. Red line is calculated from the beam-envelope equations.

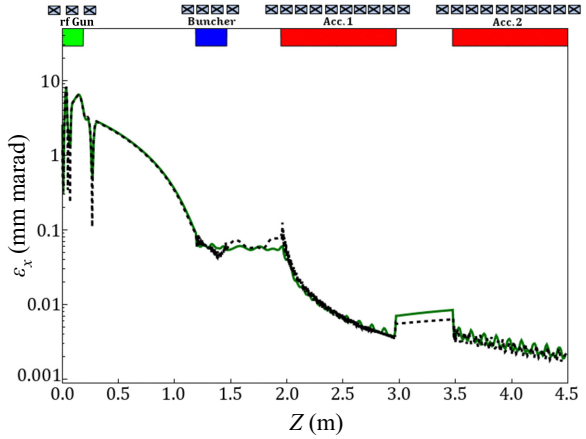


FIG. 13. Variations of the beam emittance along the AWAKE photoinjector (logarithmic scale has been applied). Black dots correspond to simulation results with ASTRA. Green line is calculated from the beam-envelope equations.

The huge space-charge effect at low energies causes the generated beam to suffer from significant quality degradation. Fortunately, this is compensated for (at least to some extent) by high-gradient rf fields excited in the rf gun. After this gun, the structure is followed by a buncher cavity and one or more accelerating structures. For bunch compression, we assume a typical CLIC $X$-band traveling-wave buncher cavity of 30 cells [48] followed by two subsequent 120-cell standard PSI traveling-wave accelerating structures [49] with the same frequencies as the buncher. To transport the beam, the whole injector is placed in a long focusing channel composed of four suitable solenoid magnets.

To design the injector, the determination of different rf-component field gradients, the drift-section lengths, and the magnetic field profile of the focusing channel is crucial. Furthermore, transferring the electron beam with a beam size free of oscillation along the injector would ensure a very small value for emittance at the final point [50]. Therefore, designing a proper focusing channel for controlling the beam size along the injector has a great impact on the final beam quality. To determine all these key parameters, we apply envelope equations [Eqs. (4) and (8)] with space-charge, emittance, and external forces, which are calculated in the previous sections, for the whole injector lattice. Then a very fast iterative method can be used instead of performing many time-consuming iterations with PIC codes, which are typically necessary for designing such an injector. These calculations lead to the direct study of the required solenoidal field for matching the beam size to a fixed function of $z$, specifying the locations and gradients of the different rf components to adjust the beam to its nominal parameters, and optimizing all structural parameters to the generation of a very-small-emittance electron beam. Our calculations show rf field gradients of 32 MeV/m for the buncher; 80 MeV/m for the two accelerating structures; and 100-, 48-, and 50-cm lengths for drifts $d_1$, $d_2$, and $d_3$, respectively, for AWAKE. Figure 10 shows the on-axis magnetic field profile of the solenoid for the AWAKE injector designed by using our model.

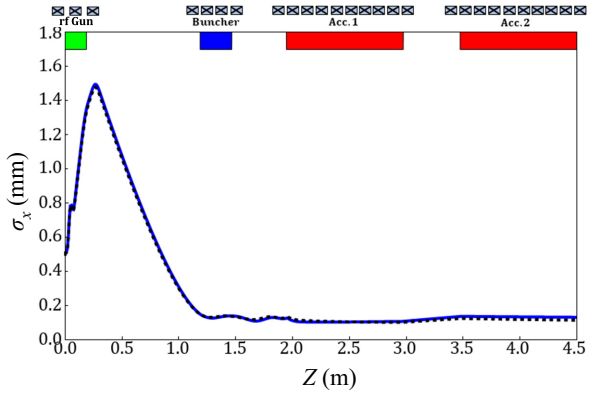


FIG. 12. Variations of the beam size along the AWAKE photoinjector. Black dots correspond to simulation results with ASTRA. Blue line is calculated from the beam-envelope equations.

The generated beam has an energy of 165.6 MeV, with $\varepsilon_{xn} = 0.46$ mm mrad, $\sigma_x = 0.11$ mm, and $\sigma_z = 60$ μm. The bunch length, beam size, and emittance variations along the designed injector are illustrated in Figs. 11–13 for analytical and simulation data. There is excellent agreement between simulations and analytical calculations.

## VI. CONCLUSION

An alternative analytical approach based on solving 6D envelope equations for studying beam dynamics in a linear accelerator structure is presented. The temporal beam evolution is investigated by analytically solving the

moment equations in both linear and nonlinear regimes. The 3D space-charge, external, and emittance forces are completely derived in terms of some simple algebraic expressions and implemented in the beam-envelope equations. For the equations to be general and very precise, the complicated effects of energy spread and emittance are included. Finally, a set of six differential equations are derived, which lead to an accurate and very fast model for simulations and designing high-current and low-emittance electron sources.

The results reveal that this analytical approach is an excellent practical choice, in terms of accuracy and time, for the calculation of beam dynamics in accelerator lines. Since this model represents an analytical approach for emittance variations, it is an efficient tool for the challenging problem of emittance compensation along injectors. Moreover, the model can be applied as a high-speed tool to calculate different bunch parameters along the whole accelerator line by the use of diagnostic data at the measurement point. This allows one to obtain much more efficient algorithms in online optimization based on machine learning. Finally, the feasibility of the presented model is demonstrated for designing the hybrid $S + X$-band photoinjector of the AWAKE.


[1] G. Ha, K. J. Kim, J. G. Power, Y. Sun, and P. Piot, Bunch shaping in electron linear accelerators, Rev. Mod. Phys. **94**, 025006 (2022).

[2] P. A. P. Nghiem, *et al.*, Toward a plasma-based accelerator at high beam energy with high beam charge and high beam quality, Phys. Rev. Accel. Beams **23**, 031301 (2020).

[3] Y. Ding, A. Brachmann, F.-J. Decker, D. Dowell, P. Emma, J. Frisch, S. Gilevich, G. Hays, Ph. Hering, Z. Huang, R. Iverson, H. Loos, A. Miahnahri, H.-D. Nuhn, D. Ratner, J. Turner, J. Welch, W. White, and J. Wu, Measurements and Simulations of Ultralow Emittance and Ultrashort Electron Beams in the Linac Coherent Light Source, Phys. Rev. Lett. **102**, 254801 (2009).

[4] E. Prat, P. Dijkstal, M. Aiba, S. Bettoni, P. Craievich, E. Ferrari, R. Ischebeck, F. Löhl, A. Malyzhenkov, G.L. Orlandi, S. Reiche, and T. Schietinger, Generation and Characterization of Intense Ultralow-Emittance Electron Beams for Compact X-Ray Free-Electron Lasers, Phys. Rev. Lett. **123**, 234801 (2019).

[5] F. Li, T. N. Dalichaouch, J. R. Pierce, X. Xu, F. S. Tsung, W. Lu, C. Joshi, and W. B. Mori, Ultrabright Electron Bunch Injection in a Plasma Wakefield Driven by a Superluminal Flying Focus Electron Beam, Phys. Rev. Lett. **128**, 174803 (2022).

[6] A. Caldwell, K. Lotov, A. Pukhov, and F. Simon, Proton-driven plasma-wakefield acceleration, Nat. Phys. **5**, 363 (2009).

[7] V. Malka, S. Fritzler, E. Lefebvre, M.-M. Aleonard, F. Burgy, J.-P. Chambaret, J.-.F Chemin, K. Krushelnick, G. Malka, S. P. D. Mangles, Z. Najmudin, M. Pittman, J.-P. Rousseau, J.-N. Scheurer, B. Walton, A. E. Dangor, Electron acceleration by a wake field forced by an intense ultrashort laser pulse, Science **298**, 1596 (2002).

[8] A. Cianchi, D. Alesini, M. P. Anania, A. Bacci, M. Bellaveglia, M. Castellano, E. Chiadroni, D. Di Giovenale, G. P. Di Pirro, M. Ferrario, A. Gallo, L. Innocenti, A. Mostacci, R. Pompili, A. R. Rossi, J. Scifo, V. Shpakov, C. Vaccarezza, and F. Villa, Six-dimensional measurements of trains of high brightness electron bunches, Phys. Rev. ST Accel. Beams **18**, 082804 (2015).

[9] Yu Bao, Gail Hanson, Robert B. Palmer, and Diktys Stratakis, Conceptual design and modeling of a six-dimensional bunch merging scheme for a muon collider, Phys. Rev. Accel. Beams **19**, 031001 (2016).

[10] PARMELA, "Phase and Radial Motion in Electron Linear Accelerators", Version 3.4, Los Alamos Accelerator Code Group, [http://laacg1.lanl.gov/], (2005).

[11] ASTRA, "A Space Charge Tracking Algorithm", Version 3.2, Notkestr.85, 22603 Hamburg, Germany, [http://www.desy.de/~mpyflo], (2017).

[12] I. Hofmann, "Space Charge Physics for Particle Accelerators", SPRINGER, ISBN 978-3-319-62157-9, (2017).

[13] M. Raiser, *"Theory and Design of Charged Particle Beams"*, 2nd ed. (Wiley-VCH Verlag GMBH, Weinheim, Germany, 2008).

[14] F. J. Sacherer, in *IEEE Trans. Nucl. Sci. NS-18* (CERN, Geneva, Switzerland, 1971), pp. 1105.

[15] M. Venturini and M. Reiser, rms Envelope Equations in the Presence of Space Charge and Dispersion, Phys. Rev. Lett. **81**, 96 (1998).

[16] J. D. Lawson, *The Physics of Charged Particle Beams* (Clarendon Press, University of Michigan, Michigan, USA, 1977).

[17] Cheng-Ying Tsai, Kuanjun Fan, Guangyao Feng, Juhao Wu, Guanqun Zhou, Yuan Hui Wu, Low-energy high-brightness electron beam dynamics based on slice beam matrix method, Nucl. Instrum. Methods Phys. Res., Sect. A **937**, 1 (2019).

[18] C. K. Allen and M. Reiser, Bunched beam envelope equations including image effects from a cylindrical pipe, Phys. Rev. E **55**, 7591 (1997).

[19] M. D. Kelisani, S. Doebert, M. Aslaninejad, B. Holzer, Evolution of bunch envelope and emittance in photo-injectors with application to the AWAKE experiment, Nucl. Instrum. Methods Phys. Res., Sect. A **982**, 164564 (2020).

[20] M. Ferrario and M. Serafini, in *Presented at VI European Particle Accelerator Conference* (Stockholm, Sweden, 1998).

[21] Luca Giannessi, Simulation codes for high brightness electron beam free-electron laser experiments, Phys. Rev. ST Accel. Beams **6**, 114802 (2003).

[22] M. Ferrario, J. E. Clendenin, D. T. Palmer, J. B. Rosenzweig, and L. Serafini, "HOMDYN Study for the LCLS rf Photo-Injector", SLAC-PUB-8400, LCLS-TN-00-04, LNF-00/004, (2000).

[23] J. P. Carneiro, N. Barov, H. Edwards, M. Fitch, W. Hartung, K. Floettmann, S. Schreiber, and M. Ferrario, Transverse and longitudinal beam dynamics studies at the fermilab photoinjector, Phys. Rev. ST Accel. Beams **8**, 040101 (2005).

[24] L. Serafini and J. B. Rosenzweig, A theory of emittance compensation, Phys. Rev. E **55**, 7565 (1997).

[25] H. Vennekate, A. Arnold, P. Lu, P. Murcek, J. Teichert, and R. Xiang, Emittance compensation schemes for a superconducting rf injector, Phys. Rev. Accel. Beams **21**, 093403 (2018).
[26] E. Adli, *et al.*, Acceleration of electrons in the plasma wakefield of a proton bunch, Nat. Phys. **561**, 363 (2018).
[27] J. D. Lawson, *The Physics of Charged-Particle Beams* (Clarendon Press, Oxford, 1977). ISBN 0-19-851278-3.
[28] R. C. Davidson and Q. Hong, *Physics of Intense Charged Particle Beams in High Energy Accelerators* (World Scientific Publishing Company, Princeton University, Princeton, USA, 2001). ISBN 13-978-1860943010.
[29] G. Sansone, *Orthogonal Functions* (Dover Publications, New York, USA, 2004). ISBN 0-486-43801-5.
[30] G. Celant and M. Broniatowski, *Interpolation and Extrapolation Optimal Design 1* (John Wiley & Sons, Hoboken, USA, 2016).
[31] L. Groening, *The Solenoids in the Bunching Section of the CTF3 Injector* (CERN, Geneva, Switzerland, 2000). CTF3 Note 2000-016.
[32] T. Gorlov, Paraxial optics of charged particles in solenoids, Phys. Rev. Accel. Beams **23**, 034001 (2020).
[33] V. Kumar, Understanding the focusing of charged particle beams in a solenoid magnetic field, Am. J. Phys. **77**, 737 (2009).
[34] S. Humphries, *Principle of Charged Particle Acceleration*, 1st ed. (Dover Publications-INC, Mineola, New York, 2012).
[35] O. Sise, M. Ulu, and M. Dogan, Characterization and modeling of multi-element electrostatic lens systems, Radiat. Phys. Chem. **76**, 593 (2007).
[36] M. Iqbal and F. E. Aleem, Theory and design of thermionic electron beam guns, AIP Conf. Proc. **748**, 376 (2005).
[37] Adam M. Darr, Caleb R. Darr, and Allen L. Garner, Theoretical assessment of transitions across thermionic, field, and space-charge-limited emission, Phys. Rev. Res. **2**, 033137 (2020).
[38] M. D. Kelisani, S. Doebert, and M. Aslaninejad, Low emittance design of the electron gun and the focusing channel of the compact linear collider drive beam, Phys. Rev. ST Accel. Beams **20**, 043403 (2017).
[39] B. M. Lewis, H. T. Tran, M. E. Read, R. L. Ives, Design of an electron gun using computer optimization, IEEE Trans. Plasma Sci. **32**, 1242 (2004).
[40] K. Wille, *"The Physics of Particle Accelerators"* (Oxford University, Oxford, UK, 1999).
[41] H. Wiedemann, *"Particle Accelerator Physics"*, 3rd ed. (Springer, Berlin, 2015).
[42] H. Wollnik, *"Optics of Charged Particles"*, 1st ed. (Academic Press, London, UK, 1987).
[43] T. P. Wangler, *rf Linear Accelerators*, 2nd ed. (John Wiley & Sons, Weinheim, Germany, 2008).
[44] C. Limborg-Deprey, C. Adolphsen, D. McCormick, M. Dunning, K. Jobe, H. Li, T. Raubenheimer, A. Vrielink, T. Vecchione, F. Wang, and S. Weathersby, Performance of a first generation *X*-band photoelectron rf gun, Phys. Rev. Accel. Beams **19**, 053401 (2016).
[45] K. Kurokawa, The expansions of electromagnetic fields in cavities, IEEE Trans. Microwave Theory Tech. **6**, 178 (1958).
[46] F. Braunmüller, *et al.*, (AWAKE Collaboration), "Proton Bunch Self-Modulation in Plasma with Density Gradient, Phys. Rev. Lett. **125**, 264801 (2020).
[47] AWAKE Design Report, "A Proton-Driven Plasma Wakefield Acceleration Experiment at CERN", CERN-SPSC-2013-013 / SPSC-TDR-003, (2013).
[48] H. Zha and A. Grudiev, Design and optimization of compact linear collider main Linac accelerating structure, Phys. Rev. ST Accel. Beams **19**, 111003 (2016).
[49] M. Dehler, in *Proc. IPAC'11* (San Sebastian, Spain, 2011).
[50] S. Bernal, R. A. Kishek, and M. Reiser, Observations and simulations of particle-density oscillations in an apertured, space-charge dominated electron beam, Proc. AIPAC **3**, 1749 (1989).